The Astrophysical Journal, 645:148–159, 2006 July 1

THE NARROW-LINE REGION OF THE SEYFERT 2 GALAXY MRK 78: AN INFRARED VIEW

C. Ramos Almeida, A. M. Pérez García, J. A. Acosta-Pulido, J. M. Rodríguez Espinosa,
R. Barrena, and A. Manchado[1]
Instituto de Astrofísica de Canarias, Vía Láctea s/n, La Laguna, E-38200 Tenerife, Spain;
cra@iac.es, apg@iac.es, jap@iac.es, jre@iac.es, rbarrena@iac.es, amt@iac.es
Received 2005 December 19; accepted 2006 March 14

ABSTRACT

We report near-infrared spectroscopic data for the Seyfert 2 galaxy Mrk 78, taken with the LIRIS near-infrared camera/spectrometer at the William Herschel Telescope (WHT). The long-slit spectra clearly show extended emission. The resolution and depth of the near-infrared spectra allow the examination of its morphology and ionization regions, and a direct comparison with similarly deep visible spectra. The emission-line ratios obtained are used to derive the extinction toward the nucleus. The detection of strong features such as [Fe II], H_2, hydrogen recombination lines, and the coronal [Si VI] λ1.962 line is used to study the kinematics and excitation mechanisms occurring in Mrk 78, revealing that despite the strong radio-jet interaction present in this object, photoionization from the active nucleus dominates the narrow-line region emission, while UV fluorescence is the source of the H_2 emission. Lines with extended emission yield velocity distributions with an amplitude of about 600 km s^{-1}, the consequence of an eastern lobe moving away from us plus a western lobe with the opposite contribution. We used the photoionization code CLOUDY to recreate a typical narrow-line region, to derive the ionization parameter, and to compare our spectral data with diagnostic diagrams.

Subject headings: galaxies: active — galaxies: individual (Mrk 78) — galaxies: nuclei — infrared: galaxies

1. INTRODUCTION

The availability of advanced near-infrared (NIR) instrumentation with panoramic arrays offers the possibility of employing diagnostic techniques that were formerly reserved for optical spectroscopy. In addition, long-slit NIR spectroscopy offers the possibility of characterizing the velocity field in active galactic nuclei (AGNs), using different line species from high-ionization emission lines (e.g., [Si VI] λ1.962), H recombination lines, Fe lines (mostly triggered by shocks), molecular H lines, or even stellar absorption features. These constitute a plethora of diagnostic tools that can be used to characterize many of the relevant phenomena acting in AGNs (regions close to the actual nucleus, partially ionized zones, the borders of molecular clouds, etc.). Furthermore, dust extinction is reduced in the IR with respect to the optical range, thus revealing lines whose optical counterparts could be obscured.

The velocity dispersions measured in the narrow emission-line region (NLR) of Seyfert galaxies are believed to be governed by the galaxy's gravitational field (Whittle 1992; Nelson & Whittle 1996). However, in a minority of Seyferts with relatively luminous linear radio sources, there is evidence for significant additional (jet-related) acceleration (Ferruit 2002; Veilleux et al. 2002). The interplay between radio-emitting flows and the line-emitting gas is important in the study of active galaxies, especially those with observable radio jets (Cecil et al. 2000, 2002; Ferruit et al. 1999). This interplay can occur in a wide range of circumstances; e.g., radio jets can be disrupted or deflected by the material in the nuclear and interstellar media. In turn, the jets can ablate, shock accelerate, destroy line-emitting clouds, or even trigger bursts of star formation. Mrk 78 is a classical example of an AGN with a jet-gas interaction, showing large bipolar flows (Whittle et al. 1988; Pedlar et al. 1989), with about half of the NLR flux originating in two components, having velocities of 680 and -480 km s^{-1}, respectively.

In this paper we present NIR long-slit data of Mrk 78 with the aim of understanding and characterizing the mechanisms responsible for its emission spectrum. Mrk 78 is a Seyfert 2 with galactic extinction amounting to $E(B-V) = 0.035$ mag (Schlegel et al. 1998). Its measured redshift ($z = 0.0371$; Michel & Huchra 1988) gives a distance of 150 Mpc and a physical scale of 715 pc arcsec^{-1} ($H_0 = 75$ km s^{-1} Mpc^{-1} is used throughout this paper). *Hubble Space Telescope* (*HST*) Wide Field Planetary Camera (WFPC) and Faint Object Camera (FOC) images taken in optical broadband filters and [O III] λ5007 emission (Capetti et al. 1994; Whittle & Wilson 2004) show a complex structure of ionized gas aligned with the radio axis at P.A. $= 84^\circ$, plus a dust lane running across the galaxy center at P.A. $= 135^\circ$ (see Fig. 1). No signs of broad emission-line region (BLR) emission have been detected from spectropolarimetry (Tran 1995). In the soft X-ray images taken by the *Röntgensatellit* (*ROSAT*) High Resolution Imager (HRI), Mrk 78 appears extended, and its spectrum can be fitted by a thermal plasma plus galactic extinction (Levenson et al. 2001).

Section 2 describes the observations, and § 3 presents the main results, covering first the nuclear emission to continue with the extended emission spectra, and the kinematics obtained from the line profiles and line displacements. Section 4 discusses the extinction toward Mrk 78 and makes an attempt at disentangling the various ionizing mechanisms at play. Finally, § 5 summarizes the main conclusions.

2. OBSERVATIONS AND DATA REDUCTION

NIR spectra in the range 0.8–2.4 μm were obtained on the night of 2005 March 22 at the 4.2 m WHT using LIRIS, a recently commissioned NIR camera/spectrometer (Manchado et al. 2004; Acosta-Pulido et al. 2003). LIRIS is equipped with a Rockwell Hawaii 1024 $\times$ 1024 HgCdTe array detector. The spatial scale is 0.″25 pixel^{-1}, and the slit width used during the

[1] Consejo Superior de Investigaciones Científicas (CSIC), Spain.

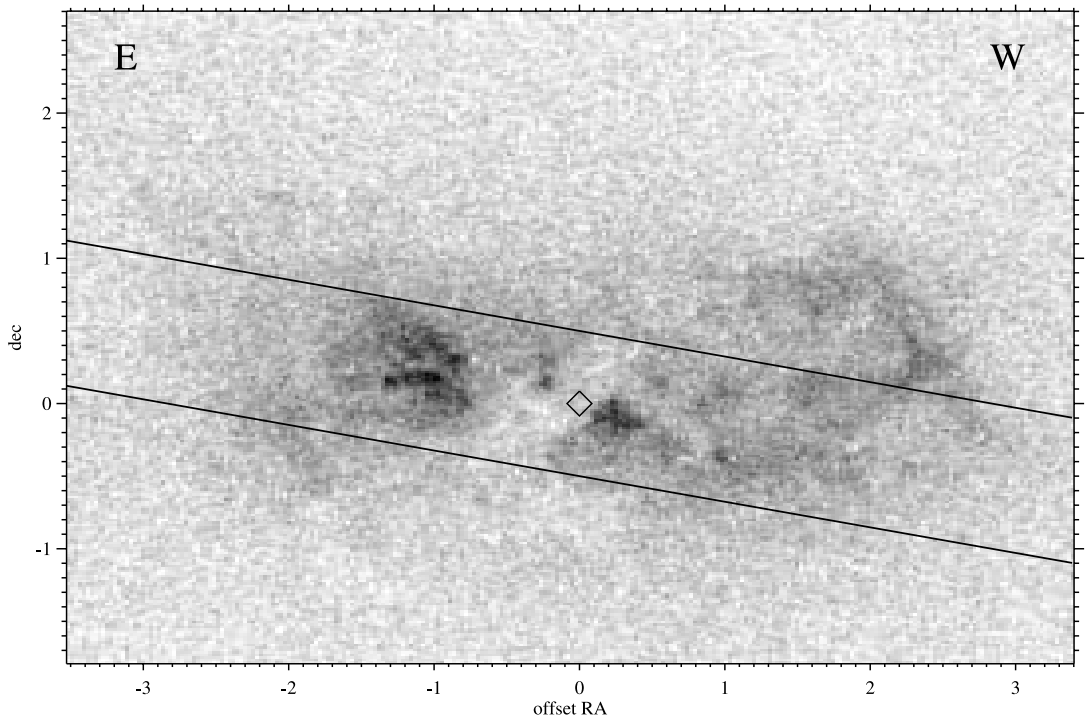

FIG. 1.— *HST* WFPC [O III] λ5007 image of Mrk 78, with the position of the LIRIS slit superimposed. The position of the brightest IR spot is marked with a diamond. The origin of the coordinate system is the same as that reported by Whittle & Wilson (2004).

observations was 1″, allowing a spectral resolution of 600 and 650 km s^{-1} in the *ZJ* and *HK* spectra, respectively. The slit was oriented along P.A. = 80°, centered on the galaxy nucleus (see Fig. 1). Weather conditions were relatively good, although with sparse cirrus. The seeing during our observations varied between 1″ and 1.″2, measured from the FWHM of the comparison stars in our NIR spectra.

Observations were performed following an ABBA telescope-nodding pattern, placing the source in two positions along the slit, separated by 15″. Individual frames were taken with integration times of 300 s and total on-source integration times of 60 minutes in each of the *ZJ* and *HK* spectra. The wavelength calibration was provided by observations of argon and xenon lamps available in the calibration unit at the A&G box of the telescope. In order to obtain the telluric correction and the flux calibration, the nearby HD 61232 A0 V star was observed with the same configuration as the galaxy. The data were reduced following standard procedures for NIR spectroscopy, using IRAF[2] and the LIRIS-QL dedicated software. Consecutive pairs of AB two-dimensional spectra were subtracted to remove the sky background. The resulting frames were then wavelength-calibrated and flat-fielded before registering and co-adding all frames to provide the final spectrum. The final wavelength-calibrated galaxy spectra were divided by a composite spectrum to remove telluric contamination. This composite spectrum was generated from the observed spectra of A0 V star HD 61232, divided by a Vega model convolved with the actual spectral resolution as described by Vacca et al. (2003). Differences in the strength of telluric features likely due to mismatch of air masses and variation of atmospheric conditions between observations of the galaxy and the reference star are taken into account using Beer's law. The IRAF task `telluric` was used in this step. The flux calibration was carried out by normalizing with the *JHK* magnitudes provided in the Two Micron All Sky Survey (2MASS) catalog.[3] The agreement in the continuum flux level in the overlap region for the *ZJ* and *HK* spectra is quite good in spectral shape and absolute value (about 15%).

3. RESULTS

3.1. *Nuclear Emission*

In order to study the nuclear emission, we have extracted a spectrum covering 1.″25 centered on the maximum of the galaxy profile. We have identified the maximum of the continuum as the position of the active nucleus and registered in the [O III] maps (see Fig. 1), as presented in Whittle & Wilson (2004). These authors have done the registration of the optical (with *HST* spatial resolution) and radio images using absolute ground-based astrometry (Clements 1981). They found a good alignment between the peak of the optical images and the position of the radio core. This fact improves confidence about the coincidence of the NIR peak with the position of their nucleus. The resulting nuclear spectra in the *ZJ*, *H*, and *K* ranges are plotted in Figures 2, 3, and 4, where the wavelength has been translated to the observer's rest frame. The most obvious features in the nuclear spectra are [S III] $\lambda\lambda$0.907, 0.953; He I λ1.083, [Fe II] $\lambda\lambda$1.256, 1.643; Paβ; Paα; and the coronal line [Si VI] λ1.962 (all wavelengths are given in μm). The recombination line Brγ is also present in the *K* band, although it appears very weak and is probably immersed in an absorption feature. For this reason, its measured flux is subject to a large uncertainty. It is noteworthy to mention that in other Seyfert 2 galaxies, e.g., NGC 2273 and NGC 4569, this line is not found (Rhee & Larkin 2005).

Emission from the H_2 molecule is clearly detected, whose most prominent lines are the transitions H_2 1–0 *S*(2) and H_2 1–0

[2] IRAF is distributed by the National Optical Astronomy Observatory, which is operated by the Association of Universities for the Research in Astronomy, Inc., under cooperative agreement with the National Science Foundation (http://iraf.noao.edu/).

[3] VizieR Online Data Catalog, II/246 (R. M. Cutri et al. 2003)

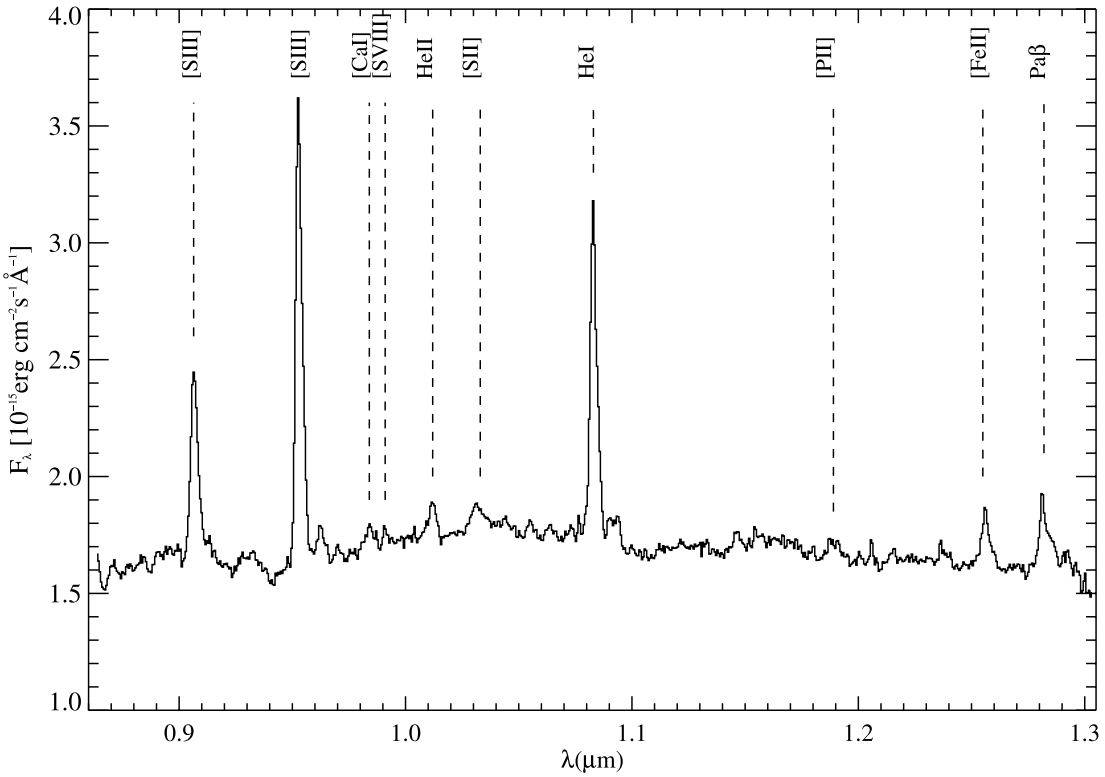

FIG. 2.— Flux-calibrated spectrum corresponding to the nuclear region of Mrk 78 within an aperture of 1″.25, taken in the *ZJ* range. Note the simultaneous detections of high- and low-ionization lines, characteristic of AGN-like spectra.

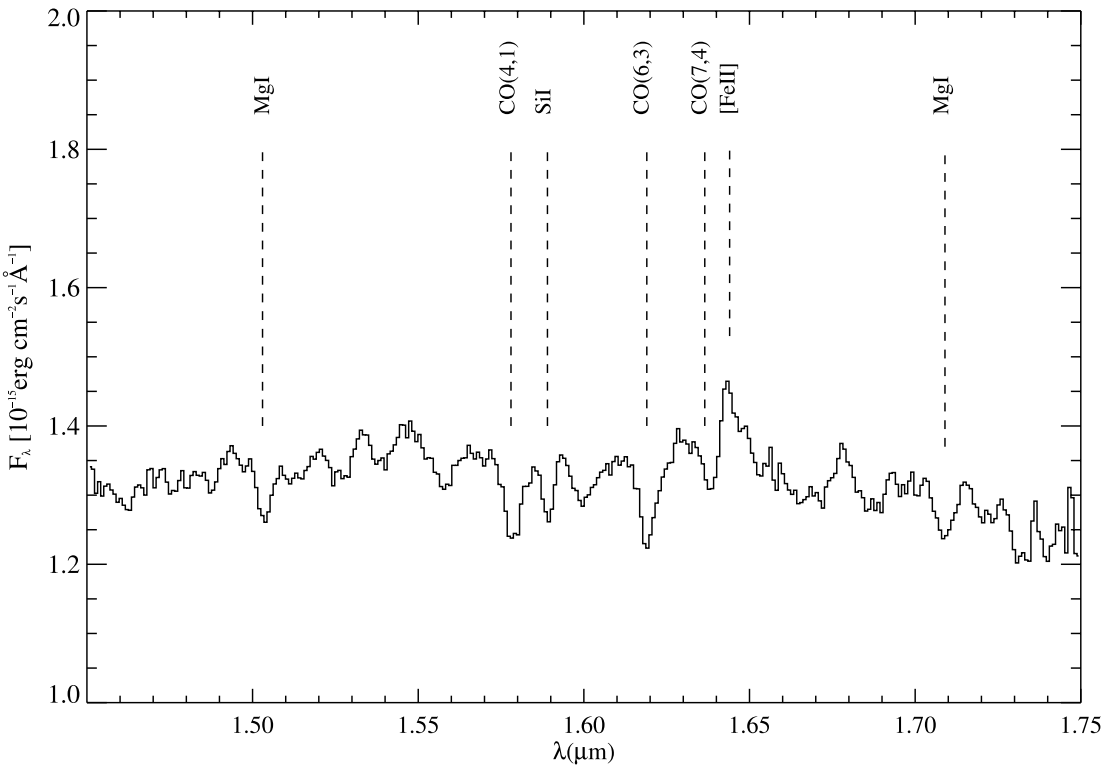

FIG. 3.— Same as Fig. 2, but in the *H* band. Note the conspicuous absorption features. This indicates a strong stellar contribution.

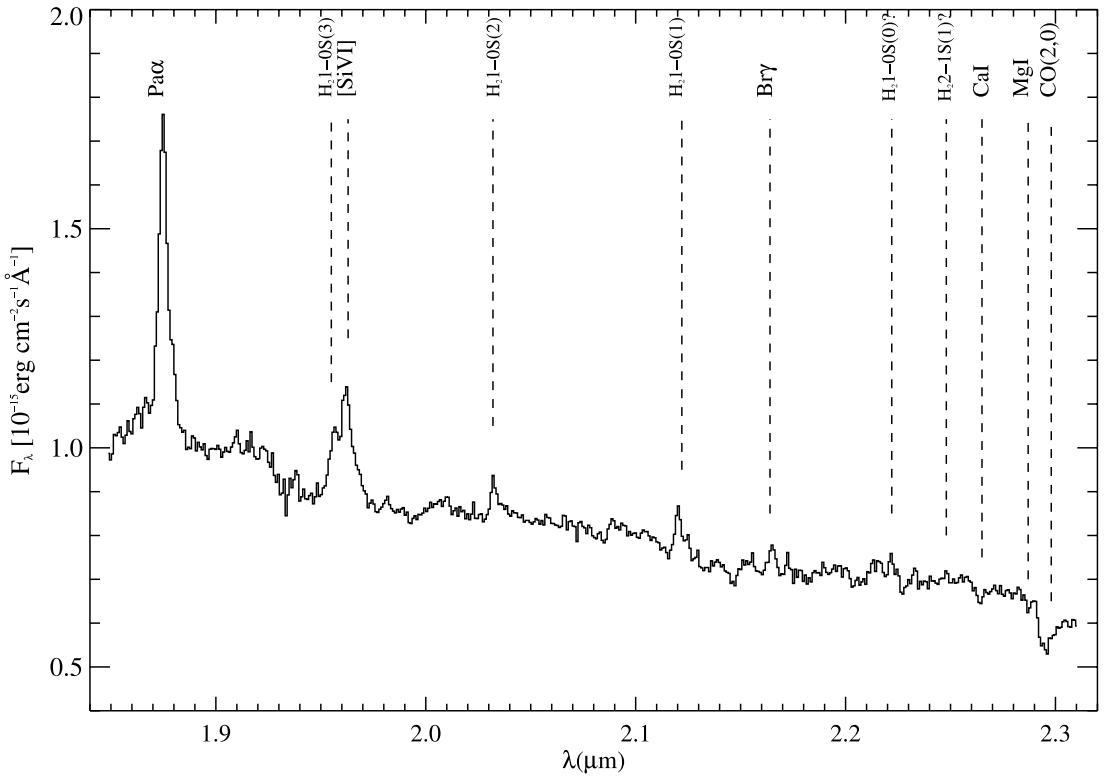

FIG. 4.— Same as Fig. 2, but in the *K* band. The most prominent line in this range is Paα; the high-ionization line [Si VI] also appears very intense, and several H_2 emission lines are clearly detected.

S(1). Both H_2 2–1 *S*(1) and H_2 1–0 *S*(0) emission lines are detected at the $\lesssim 2\ \sigma$ level.

Several other lower intensity lines are detected in the *ZJ* spectra, namely, [Ca I] λ0.985, [S VIII] λ0.991, He II λ1.012, [S II] λ1.032 (a blend of four [S II] transitions), and [P II] λ1.188, which has particular relevance as a discriminator for different excitation mechanisms of the gas (Oliva et al. 2001).

Wherever possible, all features were measured by fitting a Gaussian component using the program `twofitlines` (Acosta-Pulido 2000), developed in the IRAF environment, and the resulting values are reported in Table 1. The [Si VI] and H_2 1–0 *S*(3) lines are strongly blended, and two Gaussians were employed to separate the emission from these lines (the Starlink program DIPSO was used to perform the fits). The resulting fluxes and equivalent widths (EWs) are also reported in Table 1. The relative intensity between the H_2 1–0 *S*(3) and H_2 1–0 *S*(1) lines is 0.83, which is in good agreement with the theoretically predicted value of 1 for a wide range of conditions (Draine & Woods 1990), hence encouraging confidence concerning the deblending

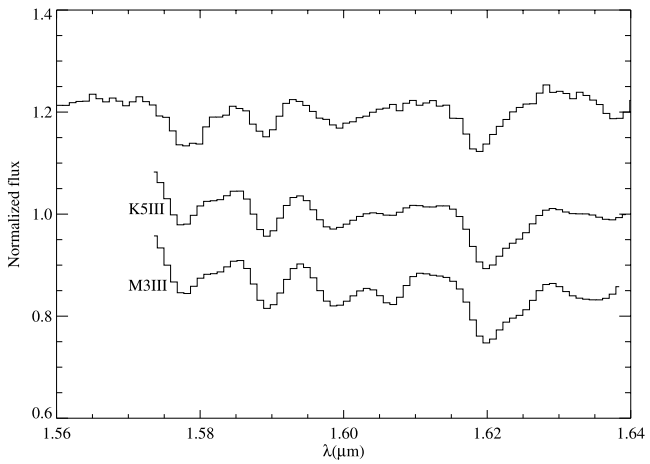

FIG. 5.— *H*-band spectra of Mrk 78 (*top line*) and two giant stars (K5 III and M3 III types). The spectra of the stars have been convolved and rebinned in order to obtain the same resolution as that of the galaxy spectrum. All spectra are normalized and shifted vertically for clarity.

TABLE 1
OBSERVED NUCLEAR EMISSION-LINE FLUXES AND EWS

Line Nucleus	λ (μm)	Flux (10^{-14} ergs cm^{-2} s^{-1})	EW (Å)
[S III]	0.907	3.54 ± 0.21	−21.5
[S III]	0.953	6.87 ± 0.21	−42.5
[Ca I]	0.985	0.39 ± 0.06	−3.03
[S VIII]	0.991	0.17 ± 0.03	−1.62
He II	1.012	0.59 ± 0.05	−3.26
[S II]	1.032	0.71 ± 0.12	−4.05
He I	1.083	5.40 ± 0.14	−31.3
[P II]	1.189	0.53 ± 0.09	−2.38
[Fe II]	1.256	0.96 ± 0.13	−5.93
Paβ	1.282	1.75 ± 0.25	−10.9
[Fe II]	1.643	0.85 ± 0.23	−6.25
Paα	1.875	4.33 ± 0.18	−40.5
H_2 1–0 S(3)	1.955	0.43 ± 0.11	−8.34
[Si VI]	1.962	1.97 ± 0.17	−17.6
H_2 1–0 S(2)	2.032	0.30 ± 0.08	−3.56
H_2 1–0 S(1)	2.121	0.52 ± 0.08	−6.88
Brγ	2.165	0.25 ± 0.02	−4.13
H_2 1–0 S(0)	2.222	:0.20	...
H_2 2–1 S(1)	2.248	:0.20	...

NOTE.—The H_2 1–0 *S*(0) and H_2 2–1 *S*(1) fluxes reported here correspond to an upper limit of 2 σ.

procedure. The [Si VI] line appears broader ($\sim$70 Å or 1100 km s^{-1}, after deconvolution), in comparison to other detected infrared lines ($\sim$600 km s^{-1}). Rodríguez-Ardila et al. (2002) claimed a trend of increasing line widths with increasing ionization potential, perhaps indicating the existence of an emission region for the coronal lines closer to the nucleus than the classical NLR.

3.1.1. *Absorption-Line Features: The Stellar Population*

Several absorption features are readily seen in the *H*-band nuclear spectrum of Mrk 78 (see Fig. 3). In particular, we observed the following ones: Mg I 1.50, CO 1.58, Si I 1.59, CO 1.62, CO 1.64, and Mg I 1.71 (all wavelengths are given in μm). These features are named according to their main contributor, although, depending on the stellar spectral type, other species may become dominant. For example, for very cool stars, OH dominates the Si I feature (Origlia et al. 1993; Dallier et al. 1996). In the *K* band, we have also detected Ca I 2.26, Mg I 2.28, and the ^{12}CO (2, 0) band head, at 2.29 μm. Unfortunately, the entire band is not included in our observations, as part of it lies outside our spectral range due to the galaxy redshift.

The ratio of the equivalent width of the 1.62 μm CO (6, 3) feature to that of the 1.59 μm Si I one is a good temperature indicator for late-type stars (Origlia et al. 1993; Förster Schreiber 2000; Ivanov et al. 2004), since the CO (6, 3) feature grows rapidly from early-K to late-M stars, while the Si I feature is only weakly dependent on stellar temperature. Moreover, dilution and reddening effects are canceled out, due to the closeness of the features in wavelength.

In order to identify the spectral types that produce the absorption features seen in the *HK* range of Mrk 78, we compare our spectra with digitally available stellar templates from Dallier et al. (1996), observed in the *H* band with a medium resolution (see Fig. 5). The equivalent width of the intrinsic stellar features has been computed after convolution of the templates, in order to match the resolution of our galaxy spectra. As a result of this comparison, for Mrk 78, the equivalent-width ratio of the CO 1.62 feature to Si I 1.59 corresponds to spectral types in the range K5 III to M3 III (see Table 2). This is consistent with results obtained by Oliva et al. (1995) for a range of galaxy types and with those of Thatte et al. (1997) for NGC 1068. An age of several hundred Myr is estimated for the stellar system, based on the fact that intermediate-to-low-mass giants dominate the integrated IR luminosity (Renzini & Buzzoni 1986).

In Seyfert galactic nuclei, these late-type stellar features are substantially diluted by nonstellar nuclear emission. Assuming a single stellar population, the dilution fraction ($D = 1 - \mathrm{EW_{obs}}/\mathrm{EW_{int}}$) can be computed from the ratio of measured to intrinsic EWs of any absorption feature (Oliva et al. 1995). Thus, in the *H* band, using the CO 1.62 feature, a starlight dilution in the range 30%–37% is obtained for the nuclear spectrum. For the *K*-band CO (2, 0) 2.29 we use, as intrinsic EWs for giant stars, those computed from the digitally available spectra from Wallace & Hinkle (1997), resulting in a dilution factor of 43%–47% in this band (see Table 2). The stellar contribution in the *J* band was estimated from the colors of K–M giants. The remaining nonstellar spectrum resembles a power law ($F_\nu \propto \nu^{-1.5}$). The index of this power law is relatively close to the average value ($F_\nu \propto \nu^{-1.35}$) claimed for the NIR pure AGN emission (Neugebauer et al. 1979), which is steeper than in the optical range.

Another common way of determining the age of the stellar population in the NIR is by means of the strength of the CO absorption feature starting at 2.29 μm. There are several working definitions of the CO index. We have used that given by Ivanov et al. (2000), which is more appropriate to the CO band measured in Mrk 78, where the spectrum ends beyond 2.31 μm. Indeed, in Mrk 78, because of its redshift, the CO band feature is close to the edge of the atmospheric window; hence, measuring the continuum level on both sides of the feature is subject to large uncertainties. The Ivanov CO index is narrower than that of Doyon et al. (1994) and has the additional advantages of being insensitive to extinction and to possible uncertainties in the continuum shape of the infrared spectra. We measure it as

$$\mathrm{CO} = -2.5 \log\left(\frac{\langle F_{2.295}\rangle}{\langle F_{2.282}\rangle}\right),$$

where $\langle F_{2.282}\rangle$ and $\langle F_{2.295}\rangle$ are the averaged flux within a bandwidth of 0.01 μm, centered on the blue continuum and at the band head, respectively. The resultant CO index is 0.149$\pm$ 0.002, which is among the lowest values obtained for Seyfert 2 galaxies by Ivanov et al. (2000), as expected because these authors used a larger spatial scale. Our value is also lower than the average one corresponding to the sample of pure starburst galaxies as reported by the same authors. Knowing the dilution factor from the nonstellar component in the *K* band, which is approximately 45%, we can estimate the CO index after removing the nonstellar contribution: 0.289 $\pm$ 0.007. In order to estimate an age from this CO index, we need to transform its value into an age-calibrated one. First, we convert our narrow spectral index into the broader, most usual one, using an expression from Ivanov et al. (2000):

$$\mathrm{CO_{Ivanov}} = (0.97 \pm 0.03)\mathrm{CO_{Doyon}} + (0.002 \pm 0.006).$$

We then obtain a photometric index using a linear relationship from Doyon et al. (1994):

$$\mathrm{CO_{spec}} = (1.46)\mathrm{CO_{phot}} - 0.02,$$

which gives a $\mathrm{CO_{phot}}$ of 0.216 $\pm$ 0.023. Looking at Figure 1 in Origlia & Oliva (2000), it is ambiguous as to which isochrone is most applicable to determine the age of the stellar population. It is well known that the CO band strength is sensitive to surface gravity and depends on both metallicity and effective temperature. For solar metallicity, the value of the index points to $\sim$30 Myr using Geneva tracks (Schaller et al. 1992), or to two different values—namely, $\sim$25 and $\sim$80 Myr—if Padua tracks (Bertelli et al. 1994) are chosen. These ambiguities have led to the use of the CO index as an age indicator being questioned. Origlia & Oliva (2000) claimed that an inadequate treatment of the asymptotic giant branch (AGB) phase produces CO features that are too weak, so the results are fairly dependent on the evolutionary tracks one adopts. Nevertheless, if late-type giants were the dominant population in the nucleus of Mrk 78, $\sim$100 Myr would be a lower limit to the age of the stellar population, and the $\sim$80 Myr

TABLE 2
Absorption Line Feature Equivalent Widths in the *H* and *K* Bands for Mrk 78 and for Three Giant Star Classes

Line	EW (Å)				Range (μm)
	Mrk 78	K5 III	M1 III	M3 III	
Si I λ1.589	2.3	2.8	2.9	2.9	1.585–1.592
CO (6, 3) λ1.619	5.1	7.8	7.3	8.1	1.614–1.627
CO (2, 0) λ2.290	8.1	14.1	15.2*	15.3	2.291–2.303

Note.—The asterisk denotes an M0 III star.

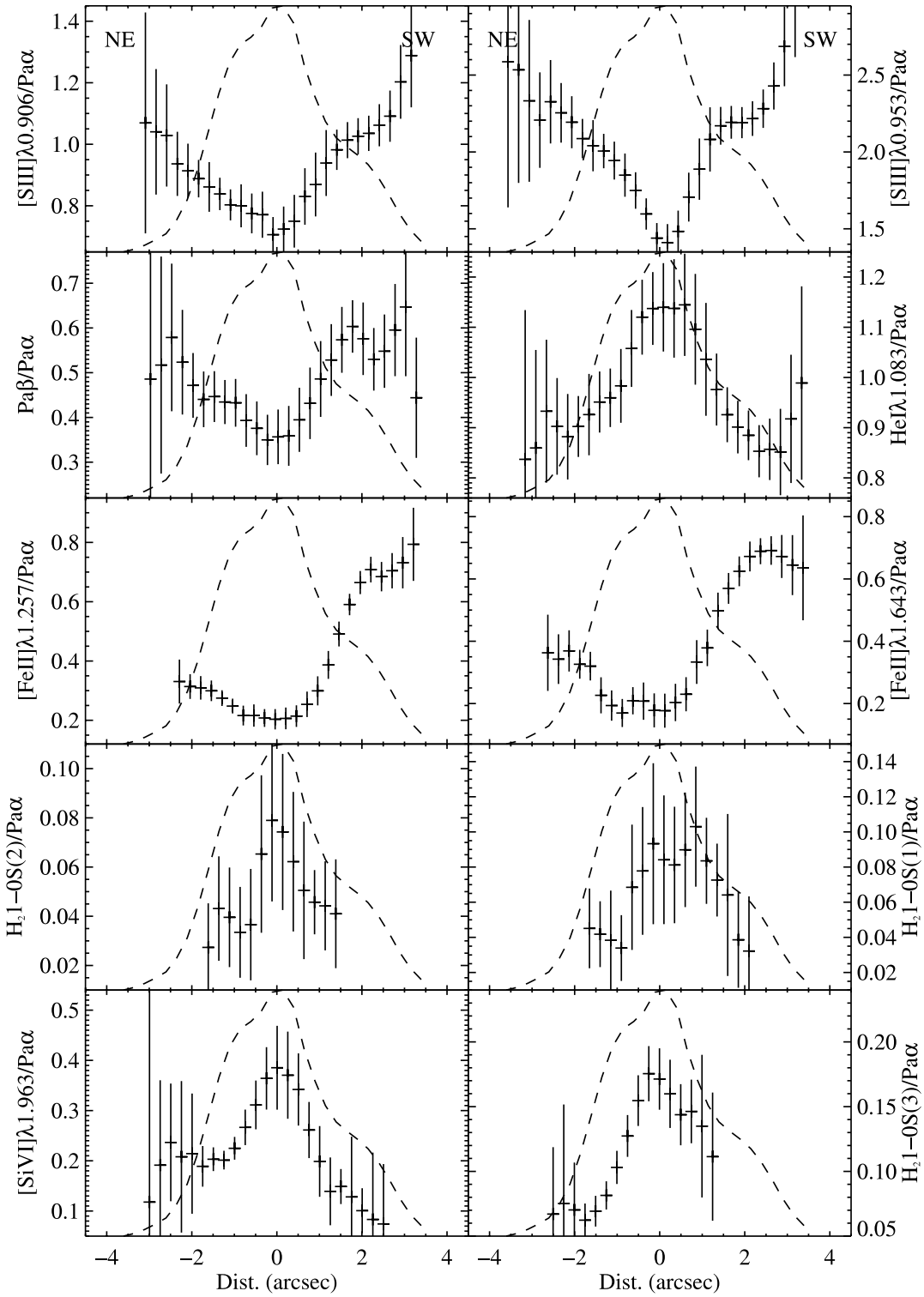

FIG. 6.—Most prominent emission line flux profiles vs. distance from the nucleus, divided by the Paα contribution. The dashed line represents the flux distribution of the Paα line on a logarithmic scale.

point would then be the only one possible for this case. In summary, we conclude that stellar features in the *H* and *K* bands are dominated by intermediate-to-low-mass giants, with an estimated age of approximately 100 Myr.

3.2. *Extended NLR*

Extended emission on both sides of the nucleus is observed along the slit, in several spectral lines, namely, in [Fe II] $\lambda\lambda$1.256, 1.643; [S III] $\lambda\lambda$0.907, 0.953; He I λ1.083; Paα; Paβ; and [Si VI] λ1.962. The emission in weaker lines such as Brγ, plus in several H_2 molecular lines, also appears extended, although it becomes difficult to measure, as they are at about the 1 σ level. The spectral features were measured by means of Gaussian fits using the in-house software utility `twofitlines` (Acosta-Pulido 2000). The spectra were extracted after co-adding three columns along the spatial direction, equivalent to 0.″75. However, in a region

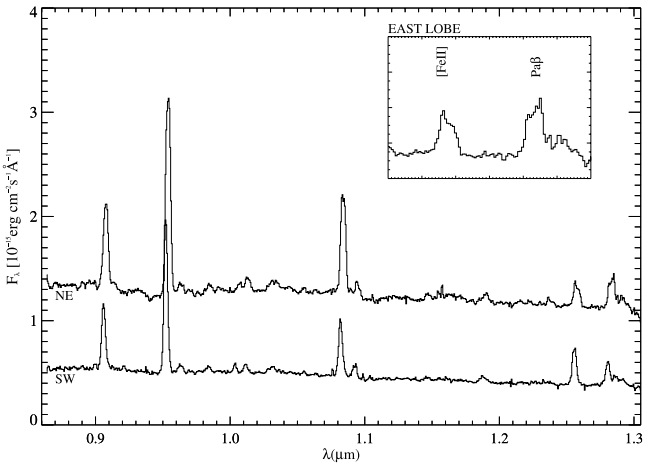

FIG. 7.—Flux-calibrated spectrum corresponding to 1.″5 to the east (*top spectrum*) and 2″ to the west (*bottom spectrum*) within an aperture of 1.″5, in the *ZJ* range. The inset shows an amplification of [Fe II] λ1.257 and Paβ double-peaked profiles in the east lobe.

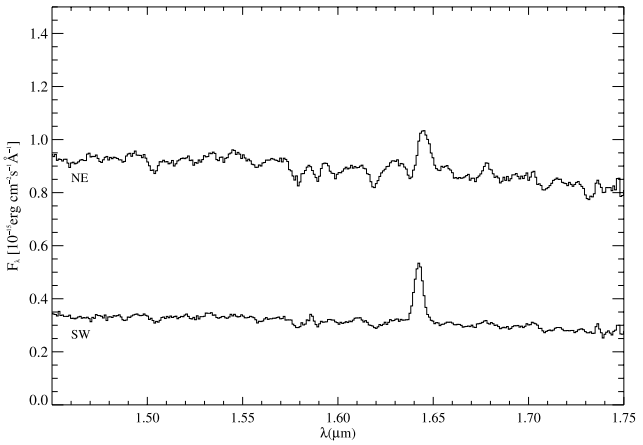

FIG. 8.—Same as Fig. 7, but in the *H* band. Note the difference in the depth of stellar features between the east and west lobes.

around 1.″5 east of the nucleus, several lines are split into two kinematic components (discussed in § 3.3). In those cases, the line fluxes are obtained by simple integration over the line profile.

Several line flux profiles are shown in Figure 6, where the Paα profile has been chosen as a baseline against which to compare the other line profiles. We note that the flux distribution of Paα is asymmetric around the nucleus. It shows first a slow decline within 1.″5 east of the nucleus and then falls steeply beyond 2″. Instead, on the opposite side of the nucleus, the profile falls quickly 1″ west of the nucleus, further showing a shoulder at ~3″. The Paα emission profile can be compared with the high spatial resolution Mrk 78 [O III] and radio images from Whittle & Wilson (2004). The radio image shows two lobes on both sides of the central nucleus, which is actually the brightest radio source. However, in [O III] radiation there are two cones of emission east and west of the center (Whittle & Wilson 2004), which is consistent with the existence of a nuclear obscuring structure. The large size of the [O III] obscured region suggests that obscuring material is required on a much larger scale, in addition to the few parsec sized torus (Pier & Krolik 1992) obscuring the active nucleus (Capetti et al. 1994). A transverse [O III] profile reveals that the emission is brighter 1.″5 to the east, decreasing toward the west after 2″, just where the Paα shows a shoulder.

The high-ionization line ratio [Si VI]/Paα shows its maximum at the position of the nucleus. It also shows an enhancement 2.″5 east of the nucleus, while it stays low (~0.1) in the western lobe. This is a clear indication that the ionization is higher in the nucleus and also in the east lobe, compared to the west side. In contrast, the [S III]/Paα line ratio shows a minimum at the nucleus and then increases to a nearly constant value in the lobes. Both these facts are indicative of a decrease in the ionization level outside the nucleus, as discussed in § 4.3.

The [Fe II]/Paα line ratio has an interesting behavior, showing a minimum at the position of the nucleus, while a high value, exceeding by a factor ~2 the value in the eastern lobe, appears in the western one. The Paβ/Paα ratio is an indicator of extinction; there are some indications that the gas in the east and west lobes does not suffer so much extinction as in the nucleus, as concluded by Whittle & Wilson (2004). The He I λ1.083/Paα ratio shows a shallow peak coincident with the nucleus of the galaxy, indicating higher ionization than in the outer nebular regions. Finally, the line ratios including H_2 indicate that the molecular emission is compact and concentrated toward the nucleus, although we cannot exclude the possibility that the molecular emission may extend in a direction perpendicular to the ionization cone as mentioned by Reunanen et al. (2003).

In summary, the scenario that we may envisage through these ratios consists of a prominent, highly ionized nucleus that is obscured by dust; an eastern lobe in which the ionization parameter is also very high according to the [Si VI] emission (a line with a very high ionization potential); and a western lobe in which the [Fe II] emission is mostly due to the higher radio-jet interaction in the west. Both lobes are less affected by extinction than the nucleus, as can be seen from the behavior of the Paβ/Paα ratio in Figure 6. This coincides with the existence of a dust band crossing the galaxy center, as can be seen in Figure 1.

3.2.1. *Eastern and Western Emission*

By looking at the variation of the line widths along the slit, we noted that there are two regions where the FWHM increases noticeably (see the discussion in § 3.3). These positions coincide with the shoulders seen in the Paα flux profile. For this reason, we decided to study these zones separately. We extracted two spectra in the *ZJ* and *HK* ranges, one centered on 1.″5 to the east, and the other 2″ to the west, covering 1.″5 (see Figs. 7–9).

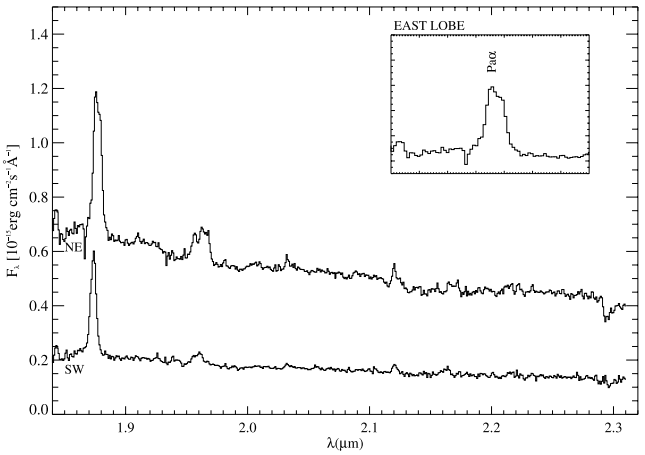

FIG. 9.—Same as Fig. 7, but in the *K* band. The inset shows an amplification of the Paα double-peaked profile in the east lobe.

TABLE 3
NUCLEAR, SOUTHWEST, AND NORTHEAST (RED AND BLUE COMPONENT) FLUXES

Line Nucleus	λ (μm)	Nuclear Emission	SW Emission	Blue NE Emission	Red NE Emission
[S III]	0.907	0.82 ± 0.08	1.02 ± 0.07	0.68 ± 0.23	1.16 ± 0.25
[S III]	0.953	1.59 ± 0.11	2.22 ± 0.13	1.45 ± 0.11	2.56 ± 0.16
He II	1.012	0.14 ± 0.02	0.12 ± 0.02	0.13 ± 0.02	0.13 ± 0.02
He I	1.083	1.25 ± 0.08	0.89 ± 0.06	1.16 ± 0.07	0.96 ± 0.07
[Fe II]	1.256	0.22 ± 0.04	0.61 ± 0.05	0.29 ± 0.04	0.22 ± 0.05
Paβ	1.282	0.40 ± 0.07	0.45 ± 0.05	0.32 ± 0.04	0.51 ± 0.06
[Fe II]	1.643	0.20 ± 0.06	0.63 ± 0.06	0.29 ± 0.04	0.15 ± 0.04
Paα	1.875	1.00	1.00	1.00	1.00
[Si VI]	1.962	0.45 ± 0.06	0.09 ± 0.04	0.24 ± 0.02	0.26 ± 0.03

NOTE.—Normalized to Paα for the most prominent lines, fitted by Gaussians.

In the east lobe, the most prominent lines (He I λ1.083, [Fe II] λ1.257, Paβ, and Paα) appeared double-peaked, as can be seen in the insets of Figures 7 and 9. The two kinematic components correspond to a blue one, which is present overall along the slit, plus a weak red component, which is only detected close to this lobe. In the west zone, the FWHM appears slightly larger than the mean value, although it is not large enough to detect more than one kinematic component.

We report integrated fluxes for the red and blue components of the eastern and western regions in Table 3. The fluxes were measured by Gaussian fitting as described in § 3.2. In the case of the east region, we employed two components, the velocity difference between them being ~600 km s^{-1}, whereas in the west region a single component was used.

The relative intensity of [Fe II] emission appears much brighter in the west; the values at the nucleus and at the east are similar. [Si VI] shows the largest value at the nucleus, and the lowest in the west lobe; intermediate and similar values are measured in the two components at the east lobe. Differences between the blue and red spectra on the east side are clearly seen in the [S III] and Paβ fluxes relative to Paα (see Table 3), showing a lower value for the blue component.

The depth of the stellar features appears very different in the east and west lobes (see Figs. 8 and 9), being much larger in the east one. Quantitatively, in the east the dilution factor is around 20%, and in the west this factor is larger than 60%, measured from the CO (2, 0) band head. Similar values are determined from the stellar absorption features in the *H* band. As expected for regions outside the nucleus, in the east lobe the stellar contribution dominates the continuum emission. In contrast, in the western lobe there could be an intense nonstellar continuum diluting the stellar counterpart, which could be related to the blue extended continuum claimed by Whittle & Wilson (2004), although its origin is still unclear. Otherwise, there could be an enhancement of old stellar population, which would contribute less to absorption features.

3.3. *Kinematics of the Ionized Gas*

A visual inspection of the two-dimensional spectrum reveals that the most intense emission lines describe what is most readily explained as a rotation curve, redshifted toward the east of the galaxy and blueshifted toward the west. Moreover, all lines appear to be resolved with an average line width of 500 km s^{-1}.

In order to analyze the velocity field, we have fitted Gaussians to the line profiles, as described in § 3.2. We note that around 1.″5 in the east and near 2″ in the west the measured line widths increase noticeably. The velocity field appears to be clearly perturbed in those regions. Furthermore, the presence of double-peaked profiles becomes evident in some of the lines around 1.″5 to the east, e.g., He I λ1.083, [Fe II] λ1.257, Paβ, and Paα (see Figs. 7 and 9). We have plotted in Figure 10 the velocity and FWHM variation along the slit. This has been done for an emission line for which we clearly distinguish two components: Paα, and for another line, the [S III] λ0.953, for which a single yet broader component

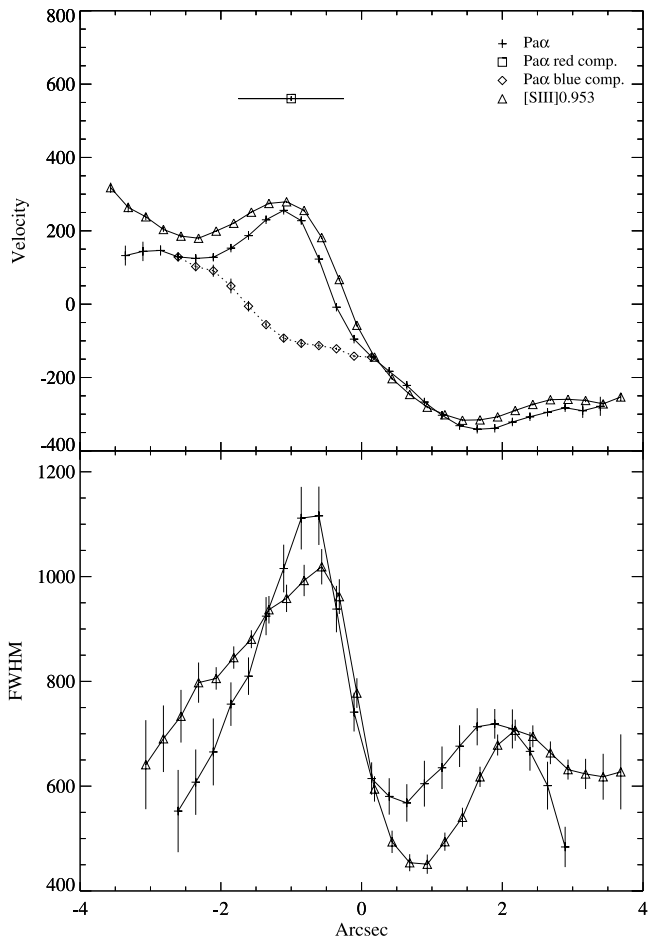

FIG. 10.—Variation of velocity and FWHM (both in km s^{-1}) measured from the lines Paα (*plus signs*) and [S III] λ0.953 (*triangles*). The overall measurements (fitted by a single Gaussian) are represented by solid lines. For the Paα, which can be split into two components, the dotted line (*diamonds*) represents the blue component, whereas the square indicates an average value for the red one.

can be fitted. In both cases, the overall behavior resembles that of a galaxy rotation curve with a half-amplitude of $\sim$300 km s^{-1}.

The Paα line profile, in the eastern lobe, can be split into two kinematic components: a blueshifted one, roughly corresponding to the nominal rotation field, and a redshifted one, with a larger mean velocity of $\sim$600 km s^{-1}, which may correspond to gas accelerated by interaction with the radio jet, as proposed by Whittle & Wilson (2004).

As stated above, the FWHM also increases at 2″ toward the west (see Fig. 10), suggesting that the gas dynamics in this region are also affected by the interaction with the radio jet. However, the spectral resolution of our spectra does not allow us to distinguish the different kinematic components.

4. DISCUSSION

4.1. *Extinction toward the Nucleus*

According to the unification scheme for Seyfert galaxies, the nucleus of Mrk 78 should be hidden from our view. This is apparently the case, as for instance Capetti et al. (1994) claimed strong obscuration toward the nucleus of Mrk 78, based on different arguments. They found that the observed UV flux is at least 3 orders of magnitude smaller than the flux required to ionize the NLR. Based on this fact, applying the reddening curve from Cardelli et al. (1989) and the standard dust-to-gas ratio, they estimated a lower limit for the column density of $N_{\rm H} > 0.5 \times 10^{22}$ cm^{-2}. They also concluded that the nuclear emission must be intrinsically anisotropic in order to explain the observed low-infrared luminosity as compared to the nuclear luminosity required to account for the overall NLR luminosity. In addition, Whittle & Wilson (2004) showed color images in which the nuclear extinction is clearly seen across several hundred parsecs. Indeed, we have not detected any broad wings in the H recombination lines present in our spectra. Previously, Goodrich et al. (1994) reported the nondetection of a broad component for Paβ in this galaxy, although their spectra have much lower signal-to-noise ratios than ours.

Moreover, the extinction toward the nucleus can be estimated from our spectra using several reddening indicators, such as the [Fe II] λ1.257 and [Fe II] λ1.644 lines, or other line ratios between the observed Paschen and Brackett H recombination lines. From these line ratios we have determined the optical extinction, A_V, using Draine's parameterization (Draine 1989), $A_\lambda \propto \lambda^{-1.75}$. The results are presented in Table 4. The [Fe II] 1.257/1.644 μm line ratio is a reliable indicator given that it is not dependent on the density or temperature of the line-emitting gas. We measured a value of 1.13 (see Table 4), which yields a moderate value for the extinction when compared to the theoretical value of 1.34 (Bautista & Pradhan 1998). The [Fe II] 1.257/1.644 line ratio measured for Mrk 78 is very close to the mean value 0.98 found in a sample of Seyfert galaxies by Rodríguez-Ardila et al. (2004). These authors argued that either the gas emission [Fe II] lines are affected by the same large extinction for most Seyfert galaxies, or the theoretical value is overestimated, given the uncertainties in the determination of the transition coefficients.

Other available reddening indicators are the Paβ/Paα and the Paα/Brγ line ratios. However, these ratios depend on the density and temperature of the line-emitting gas. In particular, the Paβ/Paα ratio varies by $\sim$8% when the temperature changes from 5000 to 20,000 K (Hummer & Storey 1987). We have adopted theoretical values corresponding to $T_e = 10{,}000$ K and $N_e = 10^4$ cm^{-3}. In our case, the observed Paα/Brγ line ratio is larger than the theoretical value. This could be due to an underestimation of the Brγ line flux, because of either the weakness of the line or an underlying absorption feature.

TABLE 4
THEORETICAL AND MEASURED EMISSION-LINE RATIOS AND A_V VALUES

Ratio	Theoretical	Measured	A_V
[Fe II] 1.26/1.64	1.34	1.13 ± 0.34	1.97
Paβ/Paα	0.49	0.40 ± 0.07	1.85
Paα/Brγ	12.2	17.3 ± 1.6	...

NOTE.—Calculated using Draine's parameterization.

The values derived for the visual extinction agree very well with those estimated by other authors using narrow emission lines (Veilleux et al. 1997; Rodríguez-Ardila et al. 2004). It is worth mentioning that the extinction measured using these narrow lines provides only an indication of the material located between us and the NLR. However, the nucleus itself and the BLR may be hidden by a larger amount of material. In fact, the nondetection of broad wings in recombination lines implies a lower limit of $A_V > 10$ (Veilleux et al. 1997), if we assume the existence of a hidden BLR.

4.2. *The Emission-Line Spectrum*

The simultaneous observation of very high and low ionization lines implies that a wide variety of physical conditions must coexist in the nuclear region of Mrk 78. This is a characteristic feature of gas photoionized by a power-law radiation source extending from the UV through X-rays. In particular, the detection of strong coronal lines such as [Si VI] λ1.962 (IP = 166.7 eV) and [S VIII] λ0.991 (IP = 280.9 eV) are indicative of the presence of extreme UV and X-ray photons (Prieto & Viegas 2000).

Marconi et al. (1994) concluded that the [Si VI] λ1.962 emission line is associated uniquely with Seyfert 1 and 2 nuclei and can only be produced by photoionization by a hard nuclear continuum. Furthermore, they indicated that this line must be produced in a dense gas with large column densities. Hot stars present in H II regions are not capable of exciting the [Si VI] line, increasing neither the ionization parameter nor the ionizing star temperature. This coronal line is therefore an excellent tracer of Seyfert activity in galaxies with visually obscured nuclei. Indeed, Oliva & Moorwood (1990) found strong [Si VI] in NGC 1068 despite the strong obscuration present in this Seyfert galaxy. Coronal lines are forbidden transitions of highly ionized species, which are formed in extreme energetic environments. Reunanen et al. (2003) observed that coronal line emission appears to be extended along the ionization cone axis, implying an anisotropic nuclear radiation field. Furthermore, coronal lines are seen with similar strength and frequency in both Seyfert types (Prieto & Viegas 2000); thus, their study provides a clean test of the unification model.

4.2.1. *The Origin of the Intense* [Fe II] *Emission*

It is well known that [Fe II] emission is weak in H II regions but strong in the shock-excited filaments of supernova remnants. In AGNs, strong [Fe II] emission is also common, although there is still some controversy about what is the dominant process responsible for this emission. Several processes may contribute to the production of the [Fe II] lines: (1) photoionization by soft X-ray extreme UV radiation from the central source, producing large, partially ionized regions in NLR clouds of high optical

depth; (2) the interaction of radio jets with the surrounding medium, which induces shocks and produces partially ionized cooling tails; and (3) fast shocks associated with supernova remnants present in starburst regions. The [Fe II] λ1.257/Paβ line ratio, or equivalently [Fe II] λ1.644/Paα, has proved to be very useful for distinguishing between a stellar and nonstellar origin for the [Fe II] emission. These line ratios increase from H II regions (photoionization) to supernovae remnants (shock excitation), passing through starburst and active galaxies (Alonso-Herrero et al. 1997; Rodríguez-Ardila et al. 2004). Galaxies with [Fe II] λ1.644/Paα[4] lower than 0.11 are classified as starbursts generally, and as LINERS if this value is larger than 0.75; Seyfert galaxies are contained in the range 0.15–0.75 (Larkin et al. 1998; Rodríguez-Ardila et al. 2004). In the case of Mrk 78, the [Fe II] λ1.644/ Paα line ratio is seen to increase outside the nucleus and shows larger values in the west lobe (see § 4.3). We found [Fe II] λ1.644/ Paα = 0.2 for the nuclear emission, and similar values in the east lobe that are well within the range of Seyfert galaxies. Those values can be explained as due to photoionization by hard UV nuclear radiation (see Fig. 12). Starburst activity is not sufficient to explain these values. In the west lobe a higher value, [Fe II] λ1.644/Paα = 0.63, was measured that is closer to the LINER locus, probably related to shock excitation, associated with a more efficient interaction with the radio jet. In order to explain the [Fe II] λ1.644/Paα line ratio in the west lobe, a composite model including shock excitation plus photoionization by the nuclear radiation is required.

On the other hand, we have detected [P II] λ1.188, which is an important emission line for discriminating between the different excitation mechanisms acting in the NLR. In particular, this line is very useful when compared with the [Fe II] λ1.257 line (Oliva et al. 2001). Both lines are produced in partially ionized regions having similar critical densities and excitation temperatures. In contrast, iron is a well-known refractory species and is strongly depleted in dust grains, whereas phosphorus is a nonrefractory species. Photoionization alone is unable to destroy the tough iron-based grains that are easily sputtered by shocks. The [Fe II]/[P II] ratio is high ($\gtrsim$20) in fast shock-excited regions, and low ($\lesssim$2) in normal photoionized regions (Oliva et al. 2001). For Mrk 78 this line ratio is 1.82 in the nuclear region, indicating that photoionization by a soft X-ray continuum is the most likely mechanism responsible for the observed nuclear spectrum.

4.2.2. *The Extended* [Fe II] *Emission and Its Relationship to Radio Emission*

As pointed out by Rodríguez-Ardila et al. (2004), the [Fe II] λ1.644/Paα line ratio is a good discriminator to discern a stellar or nonstellar origin for the [Fe II] emission, although it is not helpful in distinguishing between processes in the latter case. In addition, shocks may efficiently destroy dust grains and release iron into the gas phase, leading to an enhancement of the [Fe II] emission. An excellent way to differentiate between the different processes is the comparison of the [Fe II] emission and radio emission morphologies, despite the difficulty in obtaining [Fe II] images. Blietz et al. (1994) showed that the morphology of the [Fe II] emission correlates with that of the radio jet in NGC 1068. The most intense [Fe II] emission appears slightly offset upstream of the radio bow shock (see Fig. 2 in Blietz et al. 1994). Mrk 78 may be a similar case, in which the morphology of the [O III]-emitting gas seems to reflect different processes in the west and east lobes. The east lobe can be explained as a relatively homogeneous gas structure illuminated by the nuclear radiation source, which is penetrated by the radio emission. In contrast, the west lobe resembles a knotty gas distribution where the interaction with the radio jet has dispersed cloud fragments and swept out gas, producing compression of the gas (Whittle & Wilson 2004).

4.2.3. *The Origin of the* H_2 *Emission*

Several molecular hydrogen emission lines are present in the *K*-band spectrum of Mrk 78. These lines are clearly detected in the nucleus and in the east lobe (see Figs. 4 and 9), although the emission is mostly concentrated in the nuclear region. Reunanen et al. (2003) reported that H_2 emission is spatially resolved preferentially in directions perpendicular to the ionization cone, which is in contrast with the results reported by Quillen et al. (1999), in which H_2 emission coincides with [O III] and Hα emission.

There are three possible H_2 excitation mechanisms in galaxies: (1) UV pumping (fluorescence), (2) thermal excitation due to the presence of shocks, and (3) hard X-ray photons, which can penetrate deep into molecular clouds. These three mechanisms produce different spectral features, and the relative emission-line intensities can be used to identify the dominant mechanism. In particular, the H_2 2–1 *S*(1)/1–0 *S*(1) line ratio is lower for thermal excitation (0.1–0.2) than for UV fluorescence ($\sim$0.55), as proposed by Mouri (1994). The value obtained for the nuclear region of Mrk 78 is $\lesssim$0.38, which is larger than the predictions for pure thermal excitation, but smaller than those for nonthermal UV excitation. However, in the case of dense gas ($N_e \geq 10^4$ cm^{-3}), collisional deexcitation of the H_2 molecule modifies the spectrum, approaching the thermal spectrum. Excitation by hard X-ray is ruled out by other authors based on considerations of energetics (Rodríguez-Ardila et al. 2004) and on the detection of the transition H_2 2–1 S(3) in several Seyfert galaxies (Davies et al. 2005), which would otherwise be suppressed in the case of X-ray-irradiated gas (Davies et al. 2005).

Another way to discriminate between the thermal and fluorescent excitations is through the rotational and vibrational temperatures. In the case of thermal excitation, both temperatures should be similar, whereas in the case of fluorescent excitation a high vibrational temperature will be in contrast with a lower rotational temperature. We have determined both temperatures using the expressions given by Reunanen et al. (2002), using the H_2 line ratios 2–1 *S*(1)/1–0 *S*(1) and 1–0 *S*(0)/1–0 *S*(2). The values obtained for this galaxy are $T_{\rm vib} \lesssim 4405$ K and $T_{\rm rot} \gtrsim 1557$ K, which are in good agreement with those derived by Rodríguez-Ardila et al. (2004) for a number of Seyfert 2 galaxies, such as Mrk 279 and NGC 5728. Hence, the most likely mechanism for the excitation of H_2 in Mrk 78 is UV fluorescent in a dense gas. Note, however, that given the large uncertainties in the line flux measurements, thermal excitation cannot be ruled out.

4.3. *Comparison with Photoionization Models*

We have used the photoionization code CLOUDY (ver. C05.07.06) in order to reproduce the line ratios obtained from our spectra (for a detailed description, see Ferland 2003). We computed a grid of models based on photoionization by a power-law continuum and physical conditions in the gas typical of NLR. For the ionizing continuum we used a power-law shape of the form $f_\nu \sim \nu^\alpha$, where $\alpha = -2$ is the spectral index in the range above 10 μm. At energies below 10 μm the spectral index is $\alpha = 5/2$. We assume a plane-parallel geometry, metallicity equal

[4] We transform the [Fe II] λ1.257/Paβ line ratio to [Fe II] λ1.644/Paα using the theoretical relations for both [Fe II] and H Paschen lines. The following equation was used: [Fe II] λ1.644/Paα = 0.37[Fe II] λ1.257/Paβ.

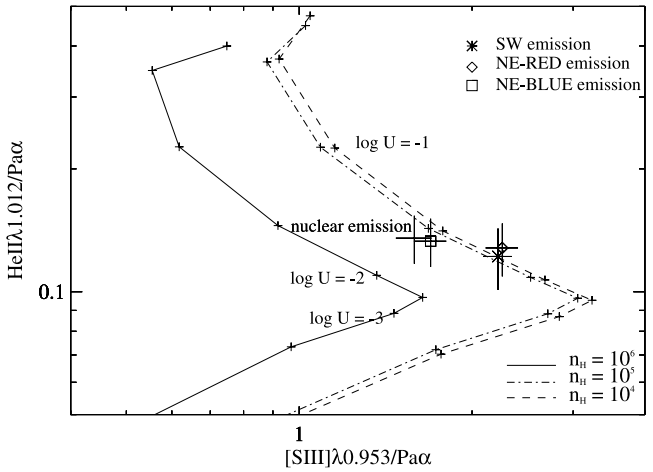

FIG. 11.—He II λ1.012/Paα vs. [S III] λ0.953/Paα diagnostic diagram computed with the photoionization code CLOUDY. Models are calculated for a power-law continuum (index -2), different values of H density (*different line types*) and a sequence of ionization parameters. The marks along the U sequence are separated by $\log U = 0.5$. Our measurements are also overplotted: cross for the nucleus, asterisk for the southwest lobe, square for the blue component in the northeast lobe, and diamond for the red component in the northeast lobe.

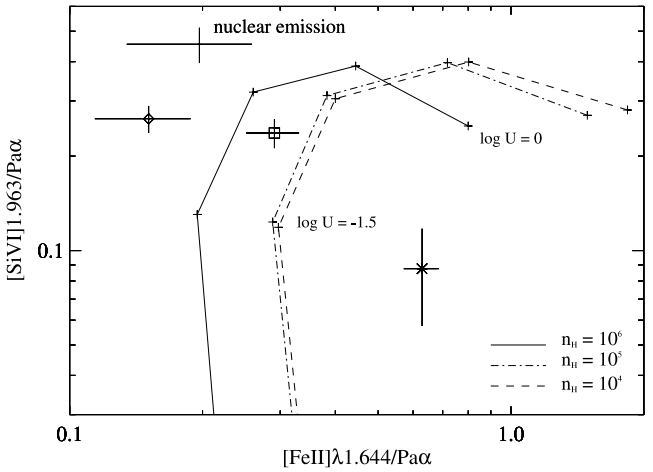

FIG. 12.—Same as Fig. 11, but with [Si VI] λ1.963/Paα vs. [Fe II] λ1.644/Paα.

to 0.3 solar, and grains with properties similar to those of the Orion Nebula, which correspond to the best-fitting models according to Alonso-Herrero et al. (1997). Three different values of hydrogen density were explored: $n_H = 10^4$, 10^5, and 10^6 cm^{-3}. An input to the code is the ionization parameter U, defined by $U = Q_H/(4\pi d^2 n_H c)$.

Line ratio diagrams are shown in Figures 11 and 12 for the following combination of lines: He II λ1.012/Paα versus [S III] λ0.953/Paα, and [Si VI] λ1.963/Paα versus [Fe II] λ1.644/Paα. Dashed lines represent the computed line ratios for the three hydrogen densities employed, beginning with an ionization parameter of $\log U = 0$ and decreasing it with a step of 0.5, toward the bottom of these plots.

Values of these line ratios from Table 3, corresponding to the nucleus, to the west lobe, and to the blue and red components of the east lobe, are overplotted for comparison with our simulations made with CLOUDY. It can be seen that data from our spectra are compatible with photoionization models for all regions considered within values of $\log U$ in the range -1 to -2, except for the [Fe II]/Paα line ratio. By looking at the diagram in Figure 11, the best fit for the nucleus and the east lobe–blue component is obtained when $\log U \sim -1.5$. However, for the west lobe and east lobe–red component, the best fit is obtained when $\log U \sim -1.8$. In all cases the H density is close to $n_H = 10^5$ cm^{-3}, which approaches the critical density for the [S III] line. From Figure 12, it is easy to see that the [Si VI]/Paα line ratio is very sensitive to the value of the ionization parameter, becoming saturated at values $\log U \sim -0.5$. At higher values of the ionization parameter, the [Si VII] λ2.480 transition will become more important. The nuclear emission can thus be explained with values $\log U \sim -0.5$, whereas in the east lobe this value decreases to $\log U \sim -1.3$, and in the west lobe to $\log U \sim -1.6$. The differences between the best-fitting values of U from the different line ratios may be reconciled by lowering the spectral index of the power law, i.e., hardening the ionizing continuum or using a combination of clouds with different optical depths. In order to explain the [Fe II]/Paα ratio, models may have to include effects due to interaction with the radio emission, such as increasing the iron abundance after grain sputtering. We therefore conclude that the measured line ratios from the spectra of Mrk 78 are compatible with photoionization by an AGN-like continuum.

5. CONCLUSIONS

We have presented and analyzed the NIR line spectrum of the nucleus and extended NLR of the Seyfert 2 galaxy Mrk 78. The following results were found:

1. The nuclear spectrum and the extended NLR spectrum are produced by photoionization by a hard UV–X-ray continuum, as indicated by the presence of the [Si VI] and [P II] lines. This fact is in good agreement with the presence of a hidden active nucleus in Mrk 78.
2. The nuclear emission in the *H* band has numerous stellar absorption features. According to the relative equivalent widths, the stellar population is dominated by K–M giants in this wavelength range. The nuclear stellar emission is diluted by a nonstellar component by a factor $\sim$34% in the *H* band and $\sim$45% in the *K* band.
3. An enhancement of the [Fe II] emission is observed outside the nucleus, in particular at $\sim 2''$ to the west. This effect is interpreted in terms of the interaction with the radio emission.
4. Several transitions of the H_2 molecule are detected in the *K* band. The dominant excitation mechanism could not be determined unambiguously, although we favor UV fluorescence in a dense gas.

We thank the anonymous referee for very useful comments that led to the improvement or our work. C. R. A., J. A. P., R. B., and A. M. acknowledge the Plan Nacional de Astronomía y Astrofísica (AYA2004-03136), which supported part of this work. The William Herschel Telescope is operated on the island of La Palma by the Isaac Newton Group in the Spanish Observatorio del Roque de los Muchachos of the Instituto de Astrofísica de Canarias. The image presented in Figure 1 is based on observations made with the NASA/ESA *Hubble Space Telescope*, obtained from the data archive at the Space Telescope Science Institute (STScI). STScI is operated by the Association of Universities for Research in Astronomy, Inc., under NASA contract NAS5-26555. The authors acknowledge the data analysis facilities provided by the Starlink Project, which is run by CCLRC on behalf of PPARC.

REFERENCES

Acosta-Pulido, J. A. 2000, in ASP Conf. Ser. 216, Astronomical Data Analysis Software and Systems IX, ed. N. Manset, C. Veillet, & D. Crabtree (San Francisco: ASP), 663
Acosta-Pulido, J. A., et al. 2003, ING Newsl., 7, 15
Alonso-Herrero, A., Rieke, M. J., Rieke, G. H., & Ruiz, M. 1997, ApJ, 482, 747
Bautista, M. A., & Pradhan, A. K. 1998, ApJ, 492, 650
Bertelli, G., Bressan, A., Chiosi, C., Fagotto, F., & Nasi, E. 1994, A&AS, 106, 275
Blietz, M., et al. 1994, ApJ, 421, 92
Capetti, A., Macchetto, F., Sparks, W. B., & Boksenberg, A. 1994, ApJ, 421, 87
Cardelli, J. A., Clayton, G. C., & Mathis, J. S. 1989, ApJ, 345, 245
Cecil, G., Dopita, M. A., Groves, B., Wilson, A. S., Ferruit, P., Pécontal, E., & Binette, L. 2002, ApJ, 568, 627
Cecil, G., et al. 2000, ApJ, 536, 675
Clements, E. 1981, MNRAS, 197, 829
Dallier, R., Boisson, C., & Joly, M. 1996, A&AS, 116, 239
Davies, R. I., Sternberg, A., Lehnert, M. D., & Tacconi-Garman, L. E. 2005, ApJ, 633, 105
Doyon, R., Joseph, R. D., & Wright, G. S. 1994, ApJ, 421, 101
Draine, B. T. 1989, in Proc. 22nd Eslab Symp., ed. B. H. Kaldeich (ESA SP-290; Noordwijk: ESA), 93
Draine, B. T., & Woods, D. T. 1990, ApJ, 363, 464
Ferland, G. J. 2003, ARA&A, 41, 517
Ferruit, P. 2002, Rev. Mex. AA Ser. Conf. 13, 183
Ferruit, P., Wilson, A. S., Falcke, H., Simpson, C., Pécontal, E., & Durret, F. 1999, MNRAS, 309, 1
Förster Schreiber, N. M. 2000, AJ, 120, 2089
Goodrich, R. W., Veilleux, S., & Hill, G. J. 1994, ApJ, 422, 521
Hummer, D. G., & Storey, P. J. 1987, MNRAS, 224, 801
Ivanov, V. D., Rieke, G. H., Groppi, E., Alonso-Herrero, A., Rieke, M. J., & Engelbracht, C. W. 2000, ApJ, 545, 190
Ivanov, V. D., Rieke, M. J., Engelbracht, C. W., Alonso-Herrero, A., Rieke, G. H., & Luhman, K. L. 2004, ApJS, 151, 387
Larkin, J. E., Armus, L., Knop, R. A., Soifer, B. T., & Matthews, K. 1998, ApJS, 114, 59
Levenson, N. A., Weaver, K. A., & Heckman, T. M. 2001, ApJS, 133, 269
Manchado, A., et al. 2004, Proc. SPIE, 5492, 1094
Marconi, A., Moorwood, A. F. M., Salvati, M., & Oliva, E. 1994, A&A, 291, 18
Michel, A., & Huchra, J. 1988, PASP, 100, 1423
Mouri, H. 1994, ApJ, 427, 777
Nelson, C. H., & Whittle, M. 1996, ApJ, 465, 96
Neugebauer, G., Oke, J. B., Becklin, E. E., & Mathews, K. 1979, ApJ, 230, 79
Oliva, E., & Moorwood, A. F. M. 1990, ApJ, 348, L5
Oliva, E., Origlia, L., Kotilainen, J. K., & Moorwood, A. F. M. 1995, A&A, 301, 55
Oliva, E., et al. 2001, A&A, 369, L5
Origlia, L., Moorwood, A. F. M., & Oliva, E. 1993, A&A, 280, 536
Origlia, L., & Oliva, E. 2000, A&A, 357, 61
Pedlar, A., et al. 1989, MNRAS, 238, 863
Pier, E. A., & Krolik, J. H. 1992, ApJ, 401, 99
Prieto, M. A., & Viegas, S. M. 2000, ApJ, 532, 238
Quillen, A. C., Alonso-Herrero, A., Rieke, M. J., Rieke, G. H., Ruiz, M., & Kulkarni, V. 1999, ApJ, 527, 696
Renzini, A., & Buzzoni, A. 1986, in Spectral Evolution of Galaxies, ed. C. Chiosi & A. Renzini (Dordrecht: Reidel), 195
Reunanen, J., Kotilainen, J. K., & Prieto, M. A. 2002, MNRAS, 331, 154
———. 2003, MNRAS, 343, 192
Rhee, J. H., & Larkin, J. E. 2005, ApJ, 620, 151
Rodríguez-Ardila, A., Pastoriza, M. G., Viegas, S., Sigut, T. A. A., & Pradhan, A. K. 2004, A&A, 425, 457
Rodríguez-Ardila, A., Viegas, S., Pastoriza, M. G., & Prato, L. 2002, ApJ, 579, 214
Schaller, G., Schaerer, D., Meynet, G., & Maeder, A. 1992, A&AS, 96, 269
Schlegel, D. J., Finkbeiner, D. P., & Davis, M. 1998, ApJ, 500, 525
Thatte, N., Quirrenbach, A., Genzel, R., Maiolino, R., & Tecza, M. 1997, ApJ, 490, 238
Tran, H. D. 1995, ApJ, 440, 565
Vacca, W. D., Cushing, M. C., & Rayner, J. T. 2003, PASP, 115, 389
Veilleux, S., Cecil, G., Bland-Hawthorn, J., & Shopbell, P. L. 2002, Rev. Mex. AA Ser. Conf. 13, 222
Veilleux, S., Goodrich, R. W., & Hill, G. J. 1997, ApJ, 477, 631
Wallace, L., & Hinkle, K. 1997, ApJS, 111, 445
Whittle, M. 1992, ApJ, 387, 109
Whittle, M., Pedlar, A., Meurs, E. J. A., Unger, S. W., Axon, D. J., & Ward, M. J. 1988, ApJ, 326, 125
Whittle, M., & Wilson, A. S. 2004, AJ, 127, 606